nanomaterials

MDPI

Article

Controllable Carbonization of Plastic Waste into Three-Dimensional Porous Carbon Nanosheets by Combined Catalyst for High Performance Capacitor

Xueying Mu [1,2], Yunhui Li [1,*], Xiaoguang Liu [3], Changde Ma [2], Hanqing Jiang [2], Jiayi Zhu [4], Xuecheng Chen [3,*], Tao Tang [2,*] and Ewa Mijowska [3]

1 School of Chemistry and Environmental Engineering, Changchun University of Science and Technology, Changchun 130022, China; xymu@ciac.ac.cn
2 State Key Laboratory of Polymer Physics and Chemistry, Changchun Institute of Applied Chemistry, Chinese Academy of Sciences, Changchun 130022, China; cdma@ciac.ac.cn (C.M.); hqjiang@ciac.ac.cn (H.J.)
3 Faculty of Chemical Technology and Engineering, West Pomeranian University of Technology, Piastow Ave. 42, 71-065 Szczecin, Poland; Xiaoguang.Liu@zut.edu.pl (X.L.); emijowska@zut.edu.pl (E.M.)
4 State Key Laboratory of Environment-friendly Energy Materials, School of Science, Southwest University of Science and Technology, Mianyang 621010, China; jyzhu@swust.edu.cn
* Correspondence: liyh@cust.edu.cn (Y.L.); xchen@zut.edu.pl (X.C.); ttang@ciac.ac.cn (T.T.); Tel.: +86-431-8558-2361 (Y.L.); +48-091-449-6030 (X.C.); +86-431-8526-2004 (T.T.)

Received: 11 May 2020; Accepted: 30 May 2020; Published: 2 June 2020

Abstract: Polyethylene terephthalate (PET) plastic has been extensively used in our social life, but its poor biodegradability has led to serious environmental pollution and aroused worldwide concern. Up to now, various strategies have been proposed to address the issue, yet such strategies remain seriously impeded by many obstacles. Herein, waste PET plastic was selectively carbonized into three-dimensional (3D) porous carbon nanosheets (PCS) with high yield of 36.4 wt%, to be further hybridized with MnO_2 nanoflakes to form PCS-MnO_2 composites. Due to the introduction of an appropriate amount of MnO_2 nanoflakes, the resulting PCS-MnO_2 composite exhibited a specific capacitance of 210.5 F g^{-1} as well as a high areal capacitance of 0.33 F m^{-2}. Furthermore, the PCS-MnO_2 composite also showed excellent cycle stability (90.1% capacitance retention over 5000 cycles under a current density of 10 A g^{-1}). The present study paved an avenue for the highly efficient recycling of PET waste into high value-added products (PCSs) for electrochemical energy storage.

Keywords: PET; waste plastic; carbonization; energy storage

1. Introduction

Due to its light weight and outstanding mechanical properties, plastic has been widely used in many fields. However, with the ever-increasing consumption of plastic products, it has flooded almost every corner of peoples' lives, and its poor biodegradability has resulted in serious environment pollution [1,2]. Currently, landfill and incineration are the most widely adopted strategies for the treatment of plastics wastes [3–5]. Nevertheless, in the long term, the decomposition of plastic waste buries underground will lead to soil and underground water contamination and harmful gases will be released into the air. However, the inappropriate treatment of plastic waste will not only cause resource waste, but also induce serious environmental pollution [6]. Although many strategies have been proposed to treat and reuse the plastic waste, it is still a great challenge to recycle the plastic waste at large scale [7]. Among various commonly used plastics, polyethylene terephthalate (PET) is widely used in our social life. For example, in China, all plastic bottles are made from PET and up to 3 million tons of PET plastic bottles are consumed every year. Therefore, developing a method for

efficient recycling of PET waste plastics has a significant impact on resources and the environment. Considering the high carbon content of PET (62.5 wt%), the transformation of PET waste into carbon materials is regarded as one of the most potentially beneficial methods due to the wide applications of carbon materials in various research fields [8]. However, the native low carbonization yield of PET seriously prohibits the implementation of this strategy as only 20 wt% of carbon material can be recycled. This is much lower than expected. Therefore, it is still a challenge to efficiently carbonize PET with high yield [9]. More importantly, it is hard to achieve controllable carbonization of PET into pre-designed nanostructures with determined physical and chemical properties [10,11].

Up to now, many research works have been published on recycling of PET waste [12–15]. For example, Elessawy et al. mixed PET waste with urea to react in autoclave reactor to prepare 3D sponge nitrogen-doped graphene [16]. The prepared N-doped graphene shows excellent specific capacitance and energy density. Kamali et al. mixed PET with NaCl with subsequent heat treatment, in which molten salt acted as a graphitization medium to improve the quality of PET plastic-derived carbon [17]. As an important energy storage device, the supercapacitor has drawn huge attention in the scientific community due to its high power density, long cycle life, and wide operating temperature range [18–20]. Although many achievements have been made, the carbonization yield is still much lower than expected. As the most essential component of the supercapacitor, the electrode material mainly determines the electrochemical performance, the exploitation of new advanced electrode materials has become the research hotspot in recent years. In general, electrode materials can be divided into three categories: carbon materials, metal oxides, and polymers [21]. Because of the excellent thermal/chemical stability, excellent conductivity, and tunable surface area, carbon materials are the most extensively studied electrode materials so far [22–25]. According to the molecular structure, the carbon content of waste PET plastic is as high as 62.5 wt%. Therefore, it is highly desired to transform PET waste into a carbon material for electrodes, which will not only reduce the environmental burden, but also provide advanced electrode materials for energy storage. It is of considerable significance to develop an efficient, time-saving, and cost-effective strategy to recycle PET waste, and more importantly, achieving controllable and high yield carbonization of PET waste simultaneously.

According to previous research, it is feasible that MgO can be used as a hard template to prepare two-dimensional carbon nanosheets, but stacking is likely to occur between carbon flakes due to π-π interaction. When cobalt acetylacetonate (III) ($Co(acac)_3$) is fully mixed with MgO flakes to form a hybrid catalyst, the resulting three-dimensional structure will not only stop the re-stacking of carbon nanosheets, but also facilitate the ion transportation within the carbon framework and further improve capacitor performance. In this contribution, waste PET bottles were used as carbon source, the hybrid $MgO/Co(acac)_3$ was used as a combined catalyst, and the porous carbon nanosheets (PCS) were selectively prepared by catalytic carbonization of PET waste. The yield of PCS was up to 36.4 wt%, which is much higher than that of neat PET carbonization product (CP) yield of 22 wt%, demonstrating the high catalytic activity of the prepared combined catalyst. MnO_2 nanoflakes were further loaded on the resulting PCSs by redox reaction to obtain hybrid PCS-MnO_2 composite, which introduced the pseudo-capacitance and further improved the capacitive performance of the hybrid material. More importantly, the PCS-MnO_2 showed an ultrahigh areal capacitance of 0.33 F m^{-2}, as well as long cycle stability [26].

2. Materials and Methods

2.1. Materials

MgO was purchased from China Guangdong Xilong Science Co., Ltd., and $Co(acac)_3$ (98%) was obtained from Aladdin Biochemical Technology Co., Ltd. (Shanghai, China). $KMnO_4$ was purchased from Beijing Chemical Plant (Beijing, China). The waste PET plastic used was a recycled waste plastic bottle. Anhydrous ethanol and HCl acid were purchased from Beijing Chemical Plant (Beijing, China), without any further purification.

2.2. Preparation of Porous Carbon Nanosheet (PCS)

Neat PET carbonization product (CP) was obtained by direct carbonization of waste PET in a reaction kettle at 700 °C. For the preparation of PCS, in the typical synthesis, MgO and $Co(acac)_3$ were put into a ball mill with a mass ratio of 2:1 to get a combined catalyst ($MgO/Co(acac)_3$). The waste PET was firstly cut into small fragments and mixed with the combined catalyst at a mass ratio of 1:2, followed by introducing into an autoclave to react at 700 °C for 1 h. Subsequently, the carbon product was taken out and refluxed in 1M HCl acid solution at 100 °C for 12 h to remove MgO and cobalt oxide from the carbon sample. In the next step, the mixture was filtered to get the PCSs sample. Finally, the PCSs were dried in vacuum at 80 °C prior to the electrochemical test.

2.3. Preparation of Porous Carbon Nanosheet (PCS-MnO_2)

To load MnO_2 nanoflakes on PCSs, in a typical synthesis, $25x$ mg (x = 1, 2, 4) of $KMnO_4$ was dissolved in 500 mL deionized water, and the solution was heated at 80 °C in an oil bath. Then 100 mg of the as-prepared carbon material (PCS) was added and stirred gently for 1 h. After cooling to room temperature, the PCS-MnO_2 composite was separated from the mixture and dried in vacuum for further use. The final composite product was denoted as PCS-MnO_2-x (x = 1, 2, 4).

2.4. Characterization

The morphology of the carbon nanomaterial was measured by a field emission scanning electron microscope (SEM, XL30ESEM-FEG) of Japan JEOL Company at an acceleration voltage of 20 kV, and the microscopic structure of the carbon nanomaterial was tested by a transmission electron microscope (TEM, JEM-1011) of Japan JEOL Company at an acceleration voltage of 100 kV. The phase composition of the carbon nanomaterial was determined by X-ray diffraction (XRD, D8 Advance X-ray diffractometer) of German Bruker Company, and the purity and thermal stability of carbon material was analyzed by a thermogravimetric analyzer (TA Instruments SDT Q600) of American TA company. The elemental composition and contents of the materials were determined by X-ray photoelectron spectroscopy (VG ESCALAB MK II) of American Thermo Scientific company at 10.0 kV and 10 mA Al Kα radiation. The N_2 adsorption/desorption isotherms were obtained at liquid nitrogen temperature (77 K) on the Micromeritics ASAP 2010 M of American Micromeritics company. The density functional theory (DFT) and Brunauer–Emmett–Teller (BET) methods were used to calculate the specific surface area and pore size distribution.

2.5. Electrochemical Test

To prepare the working electrode, in a typical synthesis, the active material, conductive carbon black, and 5 wt% of polytetrafluoroethylene (PTFE) solution were mixed together to form a paste with a mass ratio of 8:1:1, then the paste was uniformly coated on nickel foam (area: 1 cm^2), the loading amount of the active material of the obtained electrode was approximately 4 mg cm^{-2}. And then placed in a vacuum drying oven at 80 °C for 12 h. Then, a roller press was applied to press the electrode sheet to a thickness of 0.5 mm. A platinum plate was used as a counter electrode for a three-electrode test system, and 6 mol L^{-1} of KOH was used as the electrolyte. After the electrode sheet was soaked in the electrolyte for 12 h, the electrochemical tests were carried out on the electrochemical workstation (CHI 660E). Cyclic voltammetry (CV) was tested at a voltage window of −1~0 V with a scan rate of 1~200 mV s^{-1}. The galvanostatic charge-discharge (GCD) test was carried out under the test voltage window of −1~0 V and with a current density of 0.5~20 A g^{-1}. The electrochemical impedance test is in range of 0.01 Hz~100 kHz. In the three-electrode system, the gravimetric specific capacitance and the areal specific capacitance is calculated from the following equations:

$$C_{wt(CV)} = \frac{1}{2ms(V_b - V_a)} \int_{v_a}^{v_b} IdV \quad (1)$$

$$C_{wt(GCD)} = \frac{I * \Delta t}{m(V_b - V_a)} \quad (2)$$

$$C_{areal} = \frac{C_{wt(CV)}}{S_{BET}} \quad (3)$$

where $C_{wt(GCD)}$ (F g^{-1}) and $C_{wt(CV)}$ (F g^{-1}) are the gravimetric specific capacitance (C) calculated from GCD and CV results, I (A) is the current response, V_b and V_a are the high and low potential limits, m represents the carbon material mass, s (mV s^{-1}) is the scanning rate, and C_{areal} (F m^{-2}) is the areal specific capacitance, which is obtained by dividing the gravimetric specific capacitance by the specific surface area of carbon. S_{BET} (m^2 g^{-1}) is the specific surface area calculated from the N_2 adsorption and desorption (77 K) isotherm.

3. Results

The synthetic route for the preparation of PCS-MnO_2 composites is presented in Figure 1a. At the elevated temperature to 700 °C in the reactor, PET firstly decomposed into small organic molecules such as methane, ethylene, and other aromatic hydrocarbons [27]. At the same time, CoO nanoparticles were formed by the decomposition of $Co(acac)_3$ and distributed on MgO flakes evenly. Based on the decomposition–diffusion–precipitation mechanism [28], the produced small organic molecules began to deposit on the surface of CoO/MgO undergoing a dehydrogenation and aromatization reaction to form carbon layer coated on CoO/MgO [29]. After the removal of MgO and cobalt oxide species, the PCSs were finally obtained. Notably, these curved carbon nanosheets can effectively prevent carbon sheets from re-stacking process. MnO_2 nanoflakes were subsequently deposited on PCSs through the redox reaction to form PCS-MnO_2 composite [30]. The corresponding chemical reaction is shown below [31]:

$$4MnO_4^- + 3C + 3H_2O \rightarrow 4MnO_2 + CO_3^{2-} + 2HCO_3^-$$

The SEM and TEM were measured to investigate the microstructure of the obtained samples at different stages. Figure 1b, f presents the TEM and SEM images of the prepared PCS. They reveal a 3D structured porous carbon sheet with a thickness of ca. 20 nm. Figure 1c–e exhibit TEM images of PCS-MnO_2 hybrid composite. It is easy to observe that the morphology of the PCS-MnO_2 composite are the flake MnO_2 with a diameter of ca. 15 nm attached to the surface of the PCS. With the increase of the amount of $KMnO_4$ added, the amount of flake MnO_2 loaded on the PCS surface gradually enhanced from PCS-MnO_2-1 to PCS-MnO_2-4, and the thickness of MnO_2 also increased slightly. Figure 1g shows the SEM image of PCS-MnO_2-2 with the inset revealing MnO_2 nanoflakes as indicated by red circle. Supplementary Figure S1a–d presents EDX mapping of PCS-MnO_2-2. It is found that C, O, and Mn elements are evenly distributed in the measured sample.

Catalytic efficiency is one of the most important parameters to influence the applicability of the tested catalyst for carbonization of plastic waste. The obtained carbon product fabricated without adding any catalyst is in the form of carbon block (Figure 2a). The carbonization yield of this sample is only 22 wt% (see Figure 2d). When PET waste was mixed with MgO flakes, the carbonization yield increased to 25.1 wt%, slightly higher than PET itself. The morphology of this sample was in the form of flake structured carbon derivated from MgO template (Figure 2b). When only $Co(acac)_3$ was introduced to PET waste, the carbonization yield increased to 26 wt%, demonstrating slightly higher catalytic activity of $Co(acac)_3$ than MgO and PET itself. The morphology of this sample is depicted in Figure 2c. It shows core/shell structured carbon spheres. The size of carbon spheres is in the range of 20–50 nm. However, when $Co(acac)_3$ and MgO were introduced together to form a combined catalyst, the carbonization efficiency was dramatically enhanced to 36.4 wt%. This is much higher than MgO and $Co(acac)_3$ itself, further demonstrating the positive synergistic effect between $Co(acac)_3$ and MgO. The carbon product is in the form of folded flakes with rich mesopores, as shown in Figure 1b.

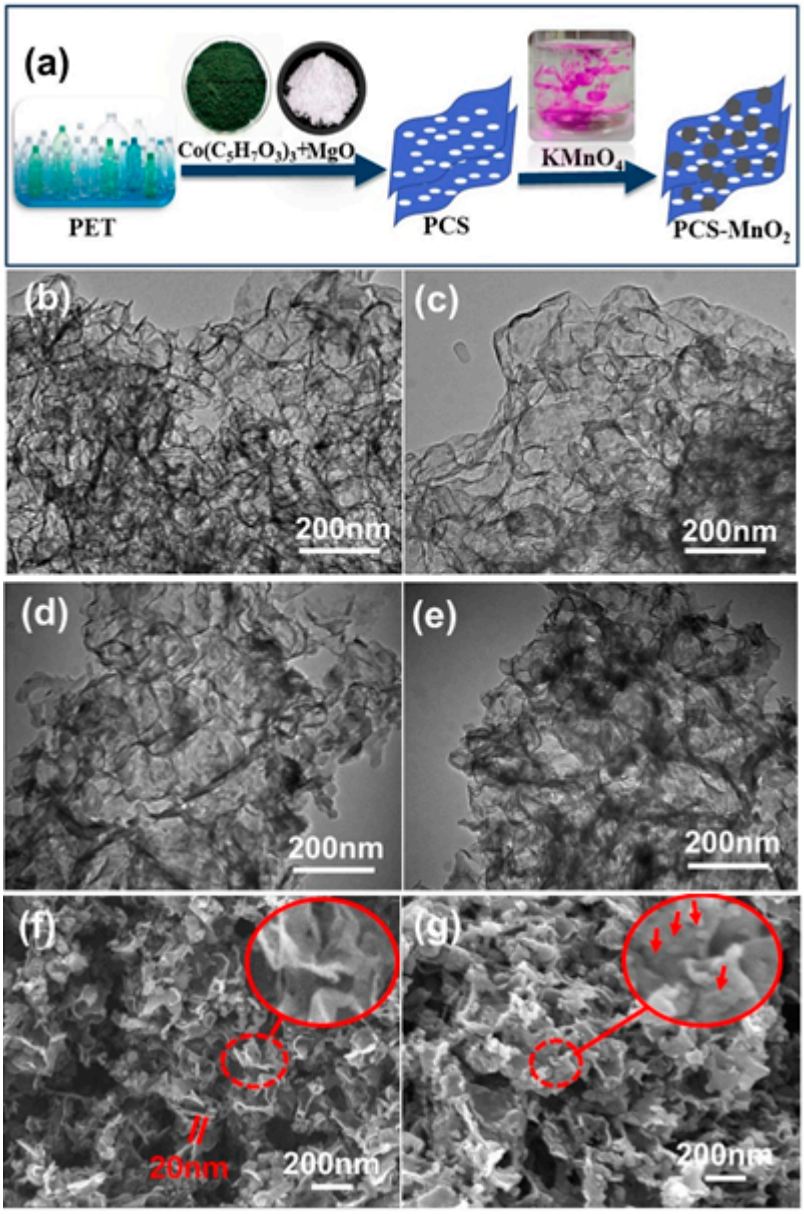

Figure 1. (**a**) Schematic illustration for the synthesis of PET waste derived PCS-MnO_2. TEM images of (**b**) PCS (**c**) PCS-MnO_2-1 (**d**) PCS-MnO_2-2 (**e**) PCS-MnO_2-4; SEM image of (**f**) PCS (**g**) PCS-MnO_2-2.

The phase composition and crystallinity of carbon samples at different stages were determined by X-ray diffraction (XRD). As observed in Figure 3a, the typical (200) peak at 43° and (220) peak at 62° are assigned to MgO (JCPDS 77-2179), which demonstrate the existence of MgO template. Besides, there are typical peaks corresponding to CoO from decomposition of $Co(acac)_3$ (JCPDS 75-0418) in the pattern. It is believed that the formed CoO with MgO synergistically promote the dehydrogenation and carbonization of the polymer when considering the carbonization yield [29,32]. In the XRD spectrum of PCS there are only two strong peaks at 26° and 43°corresponded to (002) and (101) crystal planes of hexagonal graphite [33]. In PCS-MnO_2-2, except for the peak at 26°, there are typical δ-MnO_2 (JCPDS 42-1317) peaks, which have been marked in the curves, indicating the existence of MnO_2 in the composite [34].

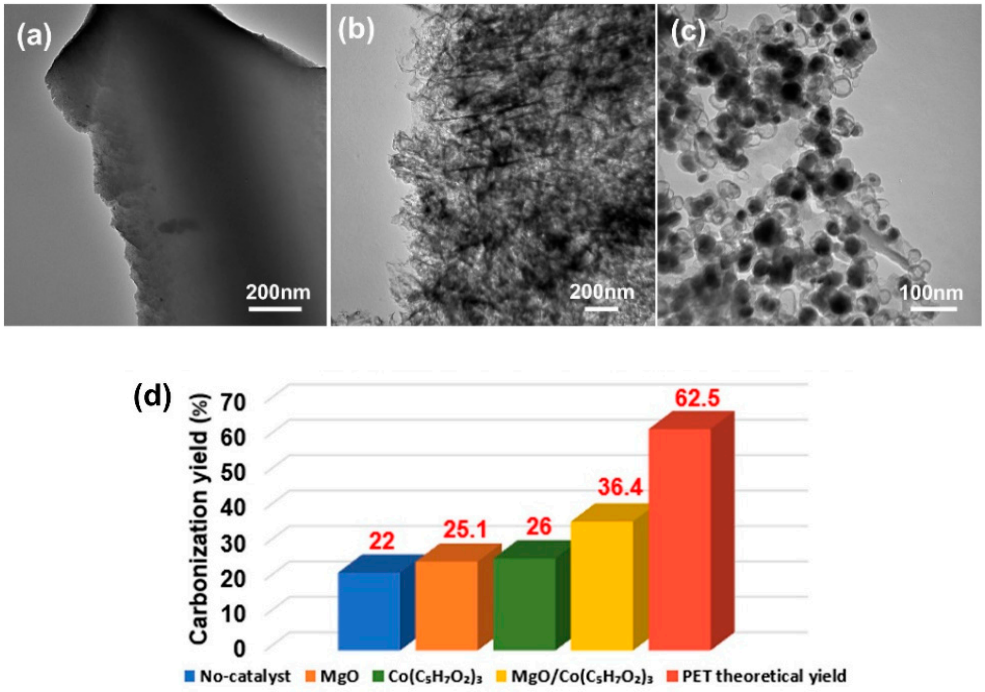

Figure 2. TEM images of (**a**) Carbon prodcut from neat PET, (**b**) Carbon sample prepared from PET/MgO, (**c**) Carbon sample from PET/Co(acac)$_3$ and (**d**) the corresponding carbon yields from different catalyst.

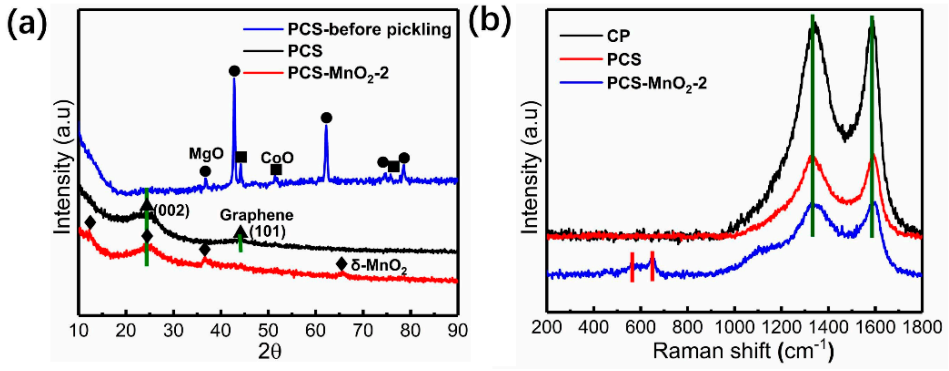

Figure 3. (**a**) XRD patterns of carbon product prepared from directly carbonized from Co(acac)$_3$/MgO/PET composite, PCS and PCS-MnO_2-2. (**b**) Raman spectra of CP, PCS and PCS-MnO_2-2.

TGA was carried out to determine the carbon content of the tested samples. All of the materials were tested under air atmosphere. As shown in Supplementary Figure S2, the amount of residual carbonized initial product is 74.4%, which indicates the amount of catalyst in the carbonized product. At 800 °C, the residue of PCS sample is 0%, implying that MgO/CoO has been completely removed from PCS. Three PCS-MnO_2 samples with different amounts of MnO_2 are clearly shown in Supplementary Figure S2. It is worth noting that the sample of PCS-MnO_2 begins to lose weight before 300 °C, which is due to the release of water trapped in the sample [35]. The weight loss in the range of 300~450 °C is due to the oxidation of PCS. In addition, due to chemical reaction of MnO_2 to Mn_2O_3, a weak weight loss is also found after 450 °C [36]. Figure 3b presents the Raman spectra of CP, PCS and PCS-MnO_2-2, respectively. All of them show two typical peaks at 1340 cm^{-1} and 1590 cm^{-1}. The D band at 1340 cm^{-1} is related to the disordered vibration peak of amorphous carbon, and the G band at 1590 cm^{-1} corresponds to the ordered carbon [37]. The ratio of I_D/I_G is used to estimate the graphitization degree of the carbon material. The higher I_D/I_G ratio implies the lower graphitization degree. According to calculation, the I_D/I_G value of CP and PCS is 1.12 and 0.99, respectively. The lower

I_D/I_G value indicates that the porous structure of PCS has a higher graphitization degree with respect to CP due to the existence of CoO inducing a higher graphitization degree. After loading of MnO_2 on PCS, the I_D/I_G value of PCS-MnO_2-2 slightly increases to 1.06, implying that the graphitization degree decreased. At the same time, two new weak peaks at 569 cm^{-1} and 641 cm^{-1} appear which correspond to δ-MnO_2 in PCS-MnO_2-2. This is consistent with the XRD result [38].

XPS analysis was used to investigate the surface chemical state of each element in the carbon samples. Supplementary Figure S3 shows XPS spectra of PCS-before HCl treatment, PCS, PCS-MnO_2-2 (a), and the narrow spectra of Mn_{2p} peaks of the PCS-MnO_2-2 (b). Supplementary Figure S3b shows high-resolution spectrum of Mn2p with the peaks at 653.8 eV and 642.2 eV corresponding to the $Mn2p_{1/2}$ and $Mn2p_{3/2}$, respectively. Moreover, the energy band of 11.6 eV between Mn2p peaks indicates the presence of δ-MnO_2, which is also in agreement with the XRD and EDX mapping results [39]. Figure 4a displays the N_2 adsorption/desorption isotherms of PCS and PCS-MnO_2 composites, respectively. Based on IUPAC specifications, lower N_2 adsorption at low relative pressure ($P/P_0 < 0.05$) and adsorption at high relative pressure ($P/P_0 > 0.9$) meet IV adsorption isotherm for two curves, indicating the abundant micropores and mesopores existed [40]. Meanwhile, the hysteresis loop in the curves also indicates the existence of mesopores. The above results are consistent with the pore size distribution analysis (Figure 4b). Figure 4b shows the numerous mesopores that exist in the PCS, which is beneficial for the ions and electrolytes free transportation within the pores. The specific surface area of PCS and PCS-MnO_2-x (x = 1, 2, 4) is reduced from 561 $m^2\ g^{-1}$ to 453 $m^2\ g^{-1}$, and the total pore volumes are 2.4 $cm^3\ g^{-1}$, 2.32 $cm^3\ g^{-1}$, 2.16 $cm^3\ g^{-1}$, and 1.86 $cm^3\ g^{-1}$, respectively. This means that the specific surface area and pore volume of PCS-MnO_2 composites decrease along with the increase in the amount of MnO_2 loading. An appropriate amount of MnO_2 loaded on PCS can not only introduce higher pseudo-capacitance to the material but also maintain a larger specific surface area and suitable pore structure, which endows the PCS-MnO_2 composite based electrode with better electrochemical performance.

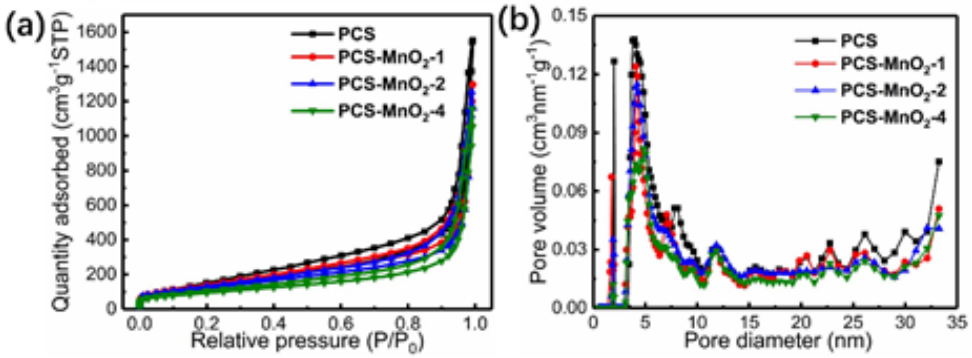

Figure 4. (**a**) N_2 adsorption/desorption isotherms and (**b**) Pore size distributions of PCS and PCS-MnO_2 composites, respectively.

A three-electrode system was first applied to investigate the electrochemical properties of the prepared carbon samples. In Figure 5a, the cyclic voltammetry (CV) curves of PCS and PCS-MnO_2 composites at 1 mV s^{-1} are shown. The rectangular-like CV curve of PCS proves its typical electric-double-layer behavior. For PCS-MnO_2 composites, there are two obvious reduction peaks from −0.4 V to −0.1 V, and another two obvious oxidation peaks in the range of −0.7 V and −0.4 V. According to previous reports, the reduction peak around −0.4 V and −0.1 V is due to the reversible redox reaction between Mn (IV) and Mn (III). While another two oxidation peaks are attributed to the oxidation reaction between Mn (III) and Mn (II) [41]. In addition, the CV integral area of PCS-MnO_2-2 is much larger than that of PCS and other PCS-MnO_2 composites. The gravimetric capacitance reaches up to 193.8 F g^{-1} at 1 mV s^{-1}, which is demonstrating that appropriate MnO_2 loading can introduce pseudo-capacitance while maintaining a large specific surface area and suitable pore structure to

improve the electrochemical performance of electrode materials. The corresponding GCD test at a current density of 1 A g^{-1} is presented in Figure 5b. Similarly, nearly triangle shape of PCS illustrates the electrochemical behavior of the electric double layer. For PCS-MnO_2 composites, there are two potential plateaus at −0.4~−0.1 V and −0.7~−0.4 V, which are consistent with the CV curves and correspond to reversible redox reaction of the transition of Mn (IV) and Mn (III), and oxidation reactions of the transition of Mn (III) and Mn (II). Among these materials, PCS-MnO_2-2 has the longest discharge time. As the loading of MnO_2 increases, the discharge time of the PCS-MnO_2 composites firstly increases and then decreases. This is due to the accumulation of MnO_2 in PCS-MnO_2-2, which reduces the utilization of MnO_2 and the ion transportation rate. The CV curves of PCS-MnO_2-2 with the scan rate in the range of 1~200 mV s^{-1} are presented in Figure 5c. The shape of the test curve remains the rectangular shape as the scan rate increases. Because of a larger specific area and suitable pore structure of PCS-MnO_2-2 composite, it guarantees the channel opened and facilitates fast ions diffusion [42]. Figure 5d shows the GCD results of PCS-MnO_2-2 at a current density of 1~20 A g^{-1}. The gravimetric capacitance is as high as 210.5 F g^{-1} at 0.5 A g^{-1}. At high current density, PCS-MnO_2-2 still shows quasi-triangular shape, which illustrates that PCS-MnO_2-2 has a good rate performance. Figure 5e shows the specific capacitance of PCS and PCS-MnO_2 composites at 1~20 A g^{-1}. Under different current densities, the specific capacitance of PCS-MnO_2-2 always remains the highest in comparison to other electrode materials. It means that PCS-MnO_2-2 contains optimal MnO_2 loading which maximizes the utilization of MnO_2 while maintaining an appropriate pore structure. These features allowed to provide an excellent electrochemical performance of this sample. Figure 5f shows the areal capacitance of graphene, PCS, and PCS-MnO_2-2 at 1 mV s^{-1}. It must be noted that the areal capacitance of PCS-MnO_2-2 is as high as 0.33 F m^{-2}, which is much higher than that of graphene (0.21 F m^{-2}) due to the introduction of pseudocapacitive reactions.

The Nyquist plots were used to investigate the kinetic characteristics of ion diffusion in the tested electrode materials. As shown in Figure 6a, there are three parts in the above Nyquist plots, the intersection with the real axis in the high-frequency region corresponding to combined series resistance (*R*s) of the materials. For PCS and three PCS-MnO_2 composites, the Rs values are 2.08 ohm, 2.23 ohm, 2.49 ohm and 2.76 ohm, indicating that when more MnO_2 is loaded on PCS, the intrinsic resistance correspondingly increases. In the mid-frequency region, the diameter of semicircle indicates the charge-transfer resistance (*R*ct) of the electrode materials [43]. The *R*ct of PCS and PCS-MnO_2 composites are 1.07 ohm, 1.38 ohm, 1.6 ohm, and 1.73 ohm, respectively. The increased amount of MnO_2 on PCS reduces the pore width of the composite materials, and enlarges the distance of ion transportation, resulting in higher charge transportation resistance. In the low-frequency region, the curves become an inclined line and nearly vertical line indicates the good ion diffusion ability of electrode materials. To measure the ion diffusion resistance, the Warburg coefficient s (ohm $s^{-1/2}$) can be extracted by fitting the real part of impedance (Z') versus the −1/2 power of the angular frequency ($w^{-1/2}$) in the low frequency range (Figure 6b) [44]. The slope of the fitted line equals the Warburg coefficient (s). The Warburg coefficient values of PCS and PCS-MnO_2 composites are 0.33 ohm $s^{-1/2}$, 0.69 ohm $s^{-1/2}$, 1.35 ohm $s^{-1/2}$, and 1.97 ohm $s^{-1/2}$, respectively. It is known that the Warburg coefficient is inversely proportional to the ion diffusion coefficient [45]. Therefore, it can be inferred from the Warburg coefficient and the change trend that abundant mesopores are beneficial for ion diffusion, and as the amount of loaded MnO_2 increases, the difficulty of ion diffusion increases. Therefore, PCS-MnO_2-2 loaded with a suitable amount of MnO_2, can maintain a suitable porous characteristic while introducing pseudo-capacitance and displays high capacitances and excellent rate capabilities. Figure 6c shows that the specific capacitance still has a retention rate of 90.1% over 5000 times GCD cycles at a current density of 10 A g^{-1}, the value is higher than those of PET-derived carbon materials previously reported (Supplementary Table S1) [46,47], which demonstrates the excellent cyclic stability of PCS-MnO_2-2 composite.

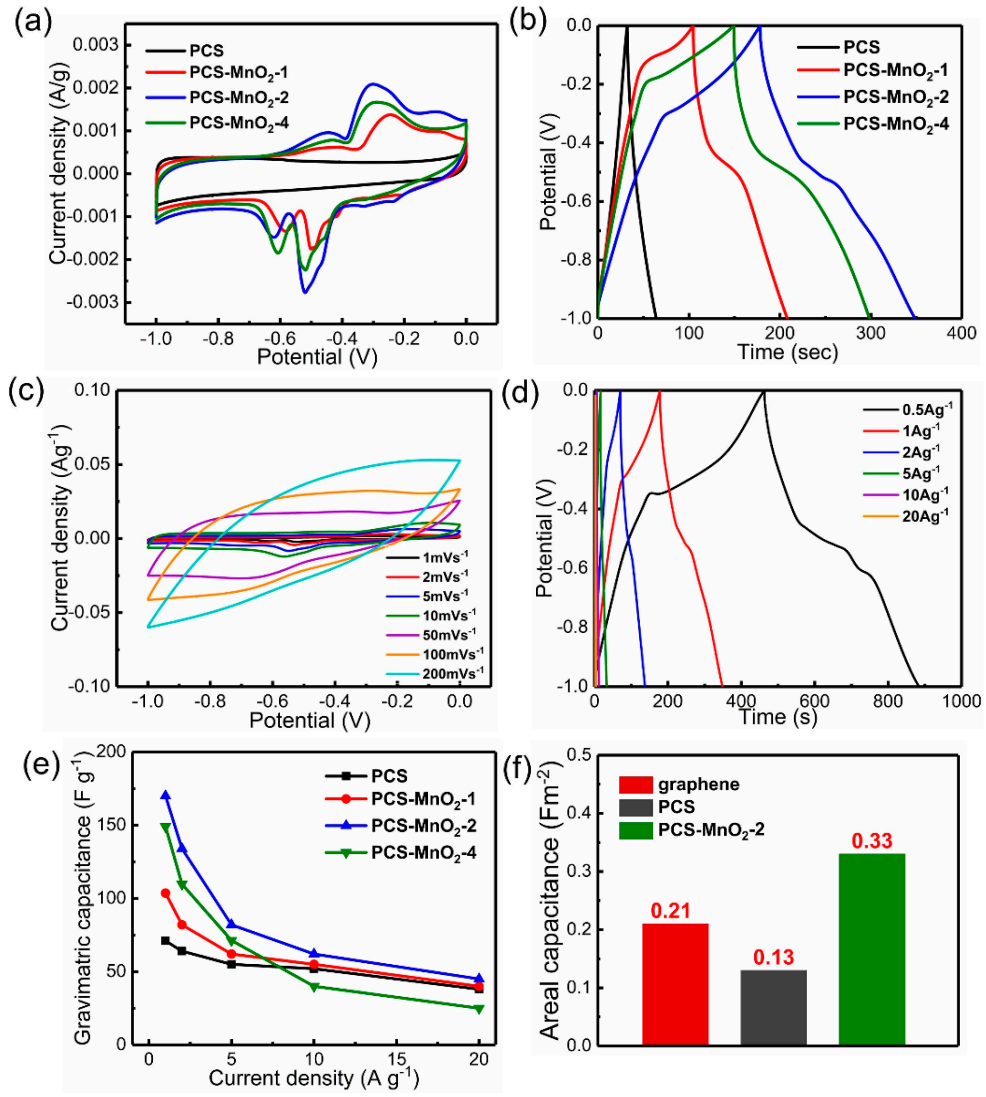

Figure 5. Electrochemical performance of PCS, PCS-MnO_2 composites in 6 M KOH electrolyte in the three-electrode test system: (**a**) CV curves tested at a scan rate of 1 mV s^{-1}, (**b**) GCD curves tested at the current density of 1 A g^{-1}. (**c**) CV curves of PCS-MnO_2-2 at the scan rate in the range of 1~200 mV s^{-1}, (**d**) GCD curves of PCS-MnO_2 at the current density in the range of 0.5~20 A g^{-1}. (**e**) The specific capacitance of PCS, PCS-MnO_2 composites at the current density in the range of 1~20 A g^{-1}. (**f**) The areal capacitance of graphene, PCS and PCS-MnO_2-2 at a scan rate of 1 mV s^{-1}.

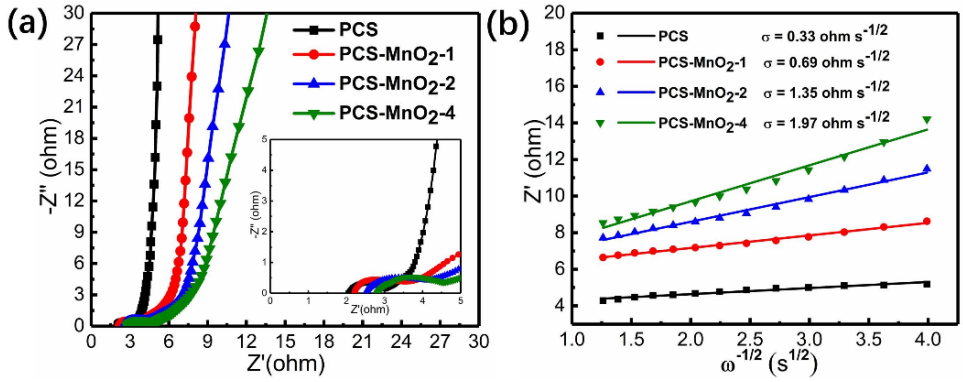

Figure 6. *Cont.*

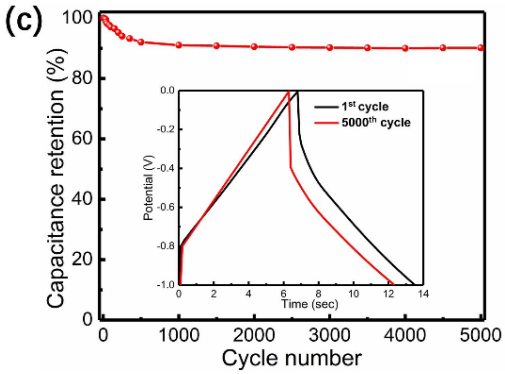

Figure 6. (**a**) The nyquist plots of PCS and PCS-MnO_2-x (x = 1, 2, 4) composites (inset: magnified semicircular part) (**b**) Linear fitting to the real part of impedance (Z′) versus the −1/2 power of the angular frequency ($w^{-1/2}$) plots in a frequency range of 0.01 Hz to 0.1 Hz to estimate the ion diffusion resistance (σ) of PCS and PCS-MnO_2 composites. (**c**) The cycling performance at 10 A g^{-1} of PCS-MnO_2-2 (inset: comparison of the first and the last charging-discharging cycle in cyclic stability test).

4. Conclusions

In summary, with the use of MgO/$Co(acac)_3$ as a template and catalyst, waste PET plastic was selectively carbonized into 3D porous carbon nanosheets with a high yield (36.4 wt%). After loading uniform MnO_2 nanoflakes on carbon nanosheets through a redox reaction, the as-prepared PCS-MnO_2-2 composite exhibited excellent capacitive performance in a supercapacitor. Due to the high specific surface area, appropriate pore size distribution, and uniformly distributed MnO_2 active sites, the PCS-MnO_2-2 composite delivered a gravimetric capacitance of 210.5 F g^{-1} and areal capacitance of 0.33 F m^{-2}, as well as excellent cycle stability. The present work demonstrates a strategy for the one-step carbonization of PET waste plastics into PCSs for energy storage, achieving the goal of recycling plastic waste into a high value-added product.

Supplementary Materials: The following are available online at http://www.mdpi.com/2079-4991/10/6/1097/s1, Figure S1. (a) SEM of PCS-MnO_2-2; EDX Mapping of (b) CKα1 (c) OKα1 (d) MnKα1; Figure S2. TGA curves of PCS-before pickling, PCS, and PCS-MnO_2 composites; Figure S3. XPS survey spectra of (a) PCS-before pickling, PCS, and PCS-MnO_2-2; (b)the narrow spectra of Mn_{2p} peaks of the PCS-MnO_2-2. Table S1. Comparison of the capacitance retention of carbon materials in the literature.

Author Contributions: X.C. designed the experiments. X.L., C.M. and H.J. administered the experiments. X.M. performed experiments. Y.L., T.T., E.M. and J.Z. gave conceptual advice. All authors analyzed and discussed the data and wrote the manuscript. All authors have read and agree to the published version of the manuscript.

Funding: This research was funded by and National Science Centre, Poland within BEETHOVEN UMO-2016/23/G/ST5/04200 and the Open Project of State Key Laboratory Cultivation Base for Nonmetal Composites and Functional Materials (grant no. 17kffk02), the Project of State Key Laboratory of Environment-friendly Energy Materials, Southwest University of Science and Technology (grant no. 18fksy0221).

Conflicts of Interest: The authors declare no conflict of interest.

References

1. Mangesh, V.L.; Padmanabhan, S.; Tamizhdurai, P.; Ramesh, A. Experimental investigation to identify the type of waste plastic pyrolysis oil suitable for conversion to diesel engine fuel. *J. Clean. Prod.* **2020**, *246*, 119066. [CrossRef]
2. Le, D.K.; Leung, R.I.H.; Er, A.S.R.; Zhang, X.W.; Tay, X.J.; Thai, Q.B.; Nhan, P.T.; Duong, H.M. Applications of functionalized polyethylene terephthalate aerogels from plastic bottle waste. *Waste Manag.* **2019**, *100*, 296–305. [CrossRef] [PubMed]
3. Wong, S.L.; Ngadi, N.; Abdullah, T.A.T.; Inuwa, I.M. Current state and future prospects of plastic waste as source of fuel: A review. *Renew. Sustain. Energy Rev.* **2015**, *50*, 1167–1180. [CrossRef]

4. Geyer, R.; Jambeck, J.R.; Law, K.L. Production, use, and fate of all plastics ever made. *Sci. Adv.* **2017**, *3*, 1700782. [CrossRef] [PubMed]
5. Hahladakis, J.N.; Iacovidou, E. An overview of the challenges and trade-offs in closing the loop of post-consumer plastic waste (PCPW): Focus on recycling. *J. Hazard. Mater.* **2019**, *380*, 120887. [CrossRef]
6. Elessawy, N.A.; Elnouby, M.; Gouda, M.H.; Hamad, H.A.; Taha, N.A.; Gouda, M.; Eldin, M.S.M. Ciprofloxacin removal using magnetic fullerene nanocomposite obtained from sustainable PET bottle wastes: Adsorption process optimization, kinetics, isotherm, regeneration and recycling studies. *Chemosphere* **2020**, *239*, 124728. [CrossRef]
7. Chen, X.; He, J.; Yan, C.; Tang, H. Novel in situ fabrication of chestnut-like carbon nanotube spheres from polypropylene and nickel formate. *J. Phys. Chem. B* **2006**, *110*, 21684–21689. [CrossRef]
8. Gong, J.; Chen, X.; Tang, T. Recent progress in controlled carbonization of (waste) polymers. *Prog. Polym. Sci.* **2019**, *94*, 1–32. [CrossRef]
9. Zhang, S.; Shi, X.; Wrobel, R.; Chen, X.; Mijowska, E. Low-cost nitrogen-doped activated carbon prepared by polyethylenimine (PEI) with a convenient method for supercapacitor application. *Electrochim. Acta* **2019**, *294*, 183–191. [CrossRef]
10. Wen, Y.; Zhang, L.; Liu, J.; Wen, X.; Chen, X.; Ma, J.; Tang, T.; Mijowska, E. Hierarchical porous carbon sheets derived on a MgO template for high-performance supercapacitor applications. *Nanotechnology* **2019**, *30*, 295703. [CrossRef]
11. Liu, X.; Ma, C.; Li, J.; Zielinska, B.; Kalenczuk, J.R.; Chen, X.; Chu, P.; Tang, T.; Mijowska, E. Biomass-derived robust three-dimensional porous carbon for high volumetric performance supercapacitors. *J. Power Sources* **2019**, *412*, 1–9. [CrossRef]
12. Liu, X.; Wen, Y.; Chen, X.; Tang, T.; Mijowska, E. Co-etching effect to convert waste polyethylene terephthalate into hierarchical porous carbon toward excellent capacitive energy storage. *Sci. Total Environ.* **2020**, *723*, 138055. [CrossRef] [PubMed]
13. Lopez, F.R.; Duque, I.I.; de Rivas, B.; Arnaiz, S.; Gutierrez, O.J.I. Chemical recycling of post-consumer PET wastes by glycolysis in the presence of metal salts. *Polym. Degrad. Stabil.* **2010**, *95*, 1022–1028. [CrossRef]
14. Ingrao, C.; Giudice, A.L.; Tricase, C.; Rana, R.; Mbohwa, C.; Siracusa, V. Recycled-PET fiber based panels for building thermal insulation: Environmental impact and improvement potential assessment for a greener production. *Sci. Total Environ.* **2014**, *493*, 914–929. [CrossRef] [PubMed]
15. Ahmadinia, E.; Zargar, M.M.; Karim, R.; Abdelaziz, M.; Ahmadinia, E. Performance evaluation of utilization of waste Polyethylene Terephthalate (PET) in stone mastic asphalt. *Constr. Build. Mater.* **2012**, *36*, 984–989. [CrossRef]
16. Elessawy, N.A.; El Nady, J.; Wazeer, W.; Kashyout, A.B. Development of High-Performance Supercapacitor based on a Novel Controllable Green Synthesis for 3D Nitrogen Doped Graphene. *Sci. Rep.* **2019**, *9*, 1129. [CrossRef]
17. Kamali, A.R.; Yang, J.G.; Sun, Q. Molten salt conversion of polyethylene terephthalate waste into graphene nanostructures with high surface area and ultra-high electrical conductivity. *Appl. Surf. Sci.* **2019**, *476*, 539–551. [CrossRef]
18. Chen, T.Y.; Vedhanarayanan, B.; Lin, S.Y.; Shao, L.D.; Sofer, Z.; Lin, J.Y.; Lin, T.W. Electrodeposited NiSe on a forest of carbon nanotubes as a free-standing electrode for hybrid supercapacitors and overall water splitting. *J. Colloid Interface Sci.* **2020**, *574*, 300–311. [CrossRef]
19. Shi, X.; Zhang, S.; Chen, X.; Tang, T.; Mijowska, E. Three dimensional graphene/carbonized metal-organic frameworks based high-performance supercapacitor. *Carbon* **2020**, *157*, 55–63. [CrossRef]
20. Zhang, S.; Shi, X.; Moszynski, D.; Tang, T.; Chu, P.K.; Chen, X.; Ewa Mijowska, E. Hierarchical porous carbon materials from nanosized metal-organic complex for high-performance symmetrical supercapacitor. *Electrochim. Acta* **2018**, *269*, 580–589. [CrossRef]
21. Ehsani, A.A.; Heidari, A.; Shiri, H.M. Electrochemical Pseudocapacitors Based on Ternary Nanocomposite of Conductive Polymer/Graphene/Metal Oxide: An Introduction and Review to it in Recent Studies. *Chem. Rec.* **2019**, *19*, 908–926. [CrossRef] [PubMed]
22. Zhai, Y.; Dou, Y.; Zhao, D.; Fulvio, P.F.; Mayes, R.T.; Dai, S. Carbon materials for chemical capacitive energy storage. *Adv. Mater.* **2011**, *23*, 4828–4850. [CrossRef] [PubMed]
23. Chen, X.; Wang, H.; He, J. Synthesis of carbon nanotubes and nanospheres with controlled morphology using different catalyst precursors. *Nanotechnology* **2008**, *19*, 325607. [CrossRef] [PubMed]

24. Cakici, M.; Reddy, K.R.; Marroquin, F.A. Advanced electrochemical energy storage supercapacitors based on the flexible carbon fiber fabric-coated with uniform coral-like MnO_2 structured electrodes. *Chem. Eng. J.* **2017**, *309*, 151–158. [CrossRef]
25. Song, M.; Zhou, Y.; Ren, X.; Wan, F.; Du, Y.; Wu, G.; Ma, F. Biowaste-based porous carbon for supercapacitor: The influence of preparation processes on structure and performance. *J. Colloid Interface Sci.* **2019**, *535*, 276–286. [CrossRef] [PubMed]
26. Dong, Y.; Zhang, S.; Du, X.; Hong, S.; Zhao, S.N.; Chen, Y.; Chen, X. Boosting the Electrical Double-Layer Capacitance of Graphene by Self-Doped Defects through Ball-Milling. *Adv. Funct. Mater.* **2019**, *29*, 1901127. [CrossRef]
27. Vouvoudi, E.C.; Achilias, D.S. Pyrolytic degradation of common polymers present in packaging materials. *J. Therm. Anal. Calorim.* **2019**, *138*, 2683–2689. [CrossRef]
28. Mattevi, C.; Kim, H.; Chhowalla, M. A review of chemical vapor deposition of graphene on copper. *J. Mater. Chem.* **2011**, *21*, 3324–3334. [CrossRef]
29. Ma, C.; Liu, X.; Min, J.; Li, J.; Gong, J.; Wen, X.; Chen, X.; Tang, T.; Mijowska, E. Sustainable recycling of waste polystyrene into hierarchical porous carbon nanosheets with potential applications in supercapacitors. *Nanotechnology* **2020**, *31*, 035402. [CrossRef]
30. Liu, T.; Zhou, Z.; Guo, Y.; Guo, D.; Liu, G. Block copolymer derived uniform mesopores enable ultrafast electron and ion transport at high mass loadings. *Nat. Commun.* **2019**, *10*, 675. [CrossRef]
31. Sun, H.; Gu, H.; Zhang, L.; Chen, Y. Redox deposition of birnessite MnO_2 on ZIF-8 derived porous carbon at room temperature for supercapacitor electrodes. *Mater. Lett.* **2018**, *216*, 123–126. [CrossRef]
32. Hong, N.; Tang, G.; Wang, X.; Hu, W.; Song, L.; Hu, Y. Selective preparation of carbon nanoflakes, carbon nanospheres, and carbon nanotubes through carbonization of polymethacrylate by using different catalyst precursors. *J. Appl. Polym. Sci.* **2013**, *130*, 1029–1037. [CrossRef]
33. Hou, J.; Cao, C.; Idrees, F.X.; Ma, L. Hierarchical Porous Nitrogen-Doped Carbon Nanosheets Derived from Silk for Ultrahigh-Capacity Battery Anodes and Supercapacitors. *ACS Nano* **2015**, *9*, 2556–2564. [CrossRef] [PubMed]
34. Zhu, X.; Dai, Y.; Sun, Y.; Liu, H.; Sun, W.; Lin, Y.; Gao, D.; Han, R.; Wang, X.; Luo, C. Rapid fabrication of electrode for the detection of alpha fetoprotein based on MnO_2 functionalized mesoporous carbon hollow sphere. *Mater. Sci. Eng. C Mater.* **2020**, *107*, 110206. [CrossRef] [PubMed]
35. Yumak, T.; Bragg, D.; Sabolsky, E.M. Effect of synthesis methods on the surface and electrochemical characteristics of metal oxide/activated carbon composites for supercapacitor applications. *Appl. Surf. Sci.* **2019**, *469*, 983–993. [CrossRef]
36. Liu, Y.H.; Hsi, H.C.; Li, K.C.; Hou, C.H. Electrodeposited Manganese Dioxide/Activated Carbon Composite as a High-Performance Electrode Material for Capacitive Deionization. *ACS Sustain. Chem. Eng.* **2016**, *4*, 4762–4770. [CrossRef]
37. Yan, J.; Fan, Z.; Wei, T.; Qian, W.; Zhang, M.; Wei, F. Fast and reversible surface redox reaction of graphene-MnO_2 composites as supercapacitor electrodes. *Carbon* **2010**, *48*, 3825–3833. [CrossRef]
38. Han, Z.; Wang, C.; Zou, X.; Chen, T.; Dong, S.; Zhao, Y.; Xie, J.; Liu, H. Diatomite-supported birnessite-type MnO_2 catalytic oxidation of formaldehyde: Preparation, performance and mechanism. *Appl. Surf. Sci.* **2020**, *502*, 144201. [CrossRef]
39. Jabeen, N.; Xia, Q.Y.; Savilov, S.V.; Aldoshin, S.M.; Yu, Y.; Xia, H. Enhanced Pseudocapacitive Performance of alpha-MnO_2 by Cation Preinsertion. *ACS Appl. Mater. Interfaces* **2016**, *8*, 33732–33740. [CrossRef]
40. Min, J.; Zhang, S.; Li, J.; Klingeler, R.; Wen, X.; Chen, X.; Zhao, X.; Tang, T.; Mijowska, E. From polystyrene waste to porous carbon flake and potential application in supercapacitor. *Waste Manag.* **2019**, *85*, 333–340. [CrossRef]
41. Xie, Y.; Yang, C.; Chen, P.; Yuan, D.; Guo, K. MnO_2-decorated hierarchical porous carbon composites for high-performance asymmetric supercapacitors. *J. Power Sources* **2019**, *425*, 1–9. [CrossRef]
42. Ghasemi, S.; Hosseini, S.R.; Boore-talari, O. Sonochemical assisted synthesis MnO_2/RGO nanohybrid as effective electrode material for supercapacitor. *Ultrason. Sonochem.* **2018**, *40*, 675–685. [CrossRef] [PubMed]
43. Hu, L.; Hou, J.; Ma, Y.; Li, H.; Zhai, T. Multi-heteroatom self-doped porous carbon derived from swim bladders for large capacitance supercapacitors. *J. Mater. Chem. A* **2016**, *4*, 15006–15014. [CrossRef]

44. Yuan, Y.; Zhan, C.; He, K.; Chen, H.; Yao, W.; Sharifi-Asl, S.; Song, B.; Yang, Z.; Nie, A.; Luo, X.; et al. The influence of large cations on the electrochemical properties of tunnel-structured metal oxides. *Nat. Commun.* **2016**, *7*, 13374. [CrossRef] [PubMed]
45. Yu, J.; Yu, C.; Guo, W.; Wang, Z.; Li, S.; Chang, J.; Tan, X.; Ding, Y.; Zhang, M.; Yang, L.; et al. Decoupling and correlating the ion transport by engineering 2D carbon nanosheets for enhanced charge storage. *Nano Energy* **2019**, *64*, 103921. [CrossRef]
46. Wen, Y.; Kierzek, K.; Chen, X.; Gong, J.; Liu, J.; Niu, R.; Mijowska, E.; Tang, T. Mass production of hierarchically porous carbon nanosheets by carbonizing "real-world" mixed waste plastics toward excellent-performance supercapacitors. *Waste Manag.* **2019**, *87*, 691–700. [CrossRef]
47. Domingo-Garcia, M.; Fernandez, J.A.; Almazan-Almazan, M.C.; Lopez-Garzon, F.J.; Stoeckli, F.; Centeno, T.A. Poly(ethylene terephthalate)-based carbons as electrode material in supercapacitors. *J. Power Sources* **2010**, *195*, 3810–3813. [CrossRef]